ACSNANO

www.acsnano.org

ARTICLE

Intrinsic Defect-Rich Hierarchically Porous Carbon Architectures Enabling Enhanced Capture and Catalytic Conversion of Polysulfides

Lu Guan, Han Hu,* Linqing Li, Yuanyuan Pan, Yifan Zhu, Qiang Li, Hailing Guo, Kai Wang, Yunchun Huang, Mengdi Zhang, Yingchun Yan, Zhongtao Li, Xiaoling Teng, Junwei Yang, Jiazhi Xiao, Yunlong Zhang, Xiaoshan Wang, and Mingbo Wu*

Cite This: *ACS Nano* 2020, 14, 6222–6231

Read Online

ACCESS | Metrics & More | Article Recommendations | Supporting Information

ABSTRACT: **Despite their promising potential, the real performance of lithium-sulfur batteries is still heavily impeded by the notorious shuttle behavior and sluggish conversion of polysulfides. Complex structures with multiple components have been widely employed to address these issues by virtue of their strong polarity and abundant surface catalytic sites. Nevertheless, the tedious constructing procedures and high cost of these materials make the exploration of alternative high-performance sulfur hosts increasingly important. Herein, we report an intrinsic defect-rich hierarchically porous carbon architecture with strong affinity and high conversion activity toward polysulfides even at high sulfur loading. Such an architecture can be prepared using a widely available nitrogen-containing precursor through a simple yet effective *in situ* templating strategy and subsequent nitrogen removal procedure. The hierarchical structure secures a high sulfur loading, while the intrinsic defects strongly anchor the active species and boost their chemical conversion because of the strong polarity and accelerated electron transfer at the defective sites. As a result, the lithium-sulfur batteries with this carbon material as the sulfur host deliver a high specific capacity of 1182 mAh g^{-1} at 0.5 C, excellent cycling stability with a capacity retention of 70% after 500 cycles, and outstanding rate capability, one of the best results among pure carbon hosts. The strategy suggested here may rekindle interest in exploring the potential of pure carbon materials for lithium-sulfur batteries as well as other energy storage devices.**

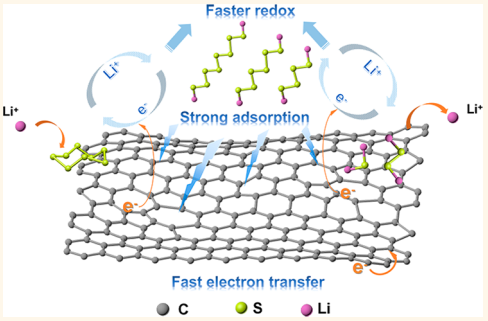

KEYWORDS: *intrinsic-carbon defects, lithium-sulfur batteries, shuttle effects, hierarchically porous carbon architectures, catalytic conversion*

To meet the surging demand of our electrified society, advanced energy storage technologies with high energy density and long service life have been actively pursued in the past decade.[1−3] Among them, lithium-sulfur (Li-S) batteries have attracted focused attention because of their high theoretical capacity, low cost, and environmental benignity of the sulfur cathode.[4−8] Nevertheless, the real performance of Li-S batteries is unsatisfactory, as the low Coulombic efficiency, poor capacity retention, and inferior calendar life are usually observed. The reasons are largely associated with the sulfur cathode regarding its insulation, formidable volume variation during operation, and the severe shuttle effect of lithium polysulfide (LiPS) intermediates.[9−13] The intrinsically insulating sulfur prevents the efficient utilization of the active species, giving a low specific capacity. Then, the lithiation-induced expansion of the cathodes generally results in pulverization of the electrode, causing rapid performance fading. The soluble LiPS intermediates shuttle between the two electrodes, which brings about deteriorated Coulombic efficiency. Moreover, the sulfur redox reactions are kinetically sluggish, resulting in notorious

Received: March 17, 2020
Accepted: April 30, 2020
Published: April 30, 2020

https://dx.doi.org/10.1021/acsnano.0c02294
ACS Nano 2020, 14, 6222–6231

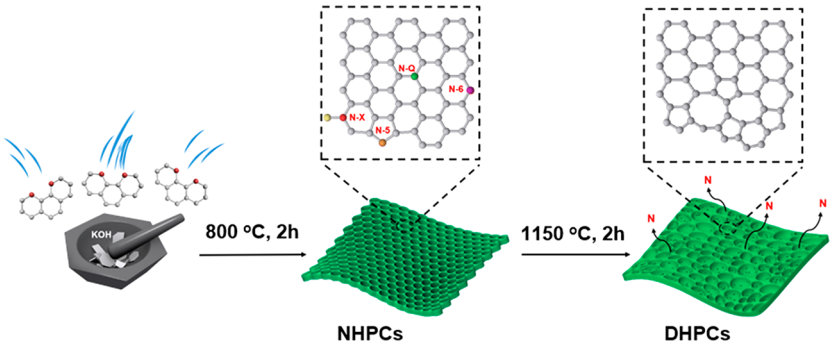

Figure 1. Schematic illustration of the synthetic process of DHPCs.

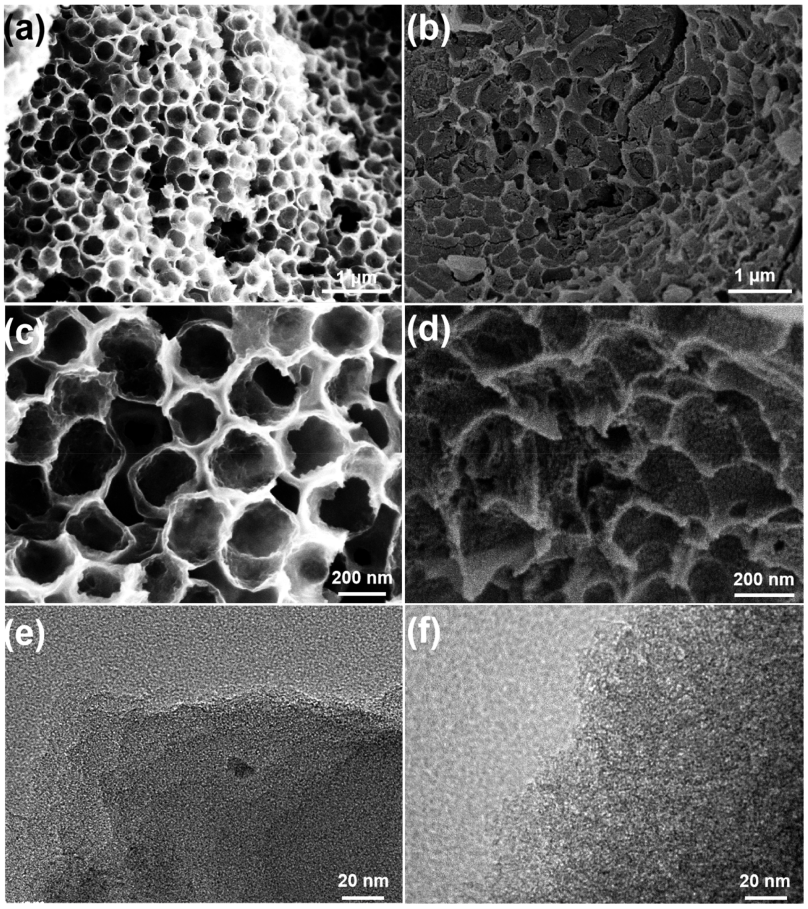

Figure 2. FESEM images of NHPCs (a, c) and DHPCs (b, d). TEM observations of NHPCs (e) and DHPCs (f).

side effects.[14] As a result, the real application of Li-S batteries remains to be a formidable challenge.

Hierarchically porous carbon architectures provide a viable solution to address the insulation and volume expansion-related issues.[15−19] The large surface area permits the uniform dispersion of sulfur that substantially shortens the diffusion path of electrons/ions *via* which the full utilization of the active species is highly possible within the conductive network. Besides, the hierarchical porosity provides sufficient space to accommodate the large volume variation during lithiation/delithiation, leading to enhanced electrode stability. Unfortunately, the nonpolar surface of carbon materials offers unfavorable affinity to the polar LiPS intermediates, failing to inhibit their shuttling.[20,21] To deal with this intractable problem, heteroatoms and/or functional groups have been anchored in the hierarchically porous carbons for enhanced adsorption of LiPSs.[22−24] However, these modification strategies afford insufficient improvements on the polarity, and the shuttle effect is thus incapable of being essentially overcome. As a result, transition-metal compounds with much higher polarity have been suggested to functionalize the porous carbon skeletons for improved LiPSs capture.[25−32] Interestingly, some of these compounds could further lead to catalytic conversion of the LiPSs, thus fundamentally boosting the performance of Li-S batteries.[33−36] To produce such hybrid compounds, tedious procedures have to be used, which increase the cost of the sulfur cathodes. Considering the large deployment of energy storage devices in the near future, it will be more appealing if the cost-effective hierarchically porous carbon architectures could be directly endowed with

https://dx.doi.org/10.1021/acsnano.0c02294
ACS Nano 2020, 14, 6222−6231

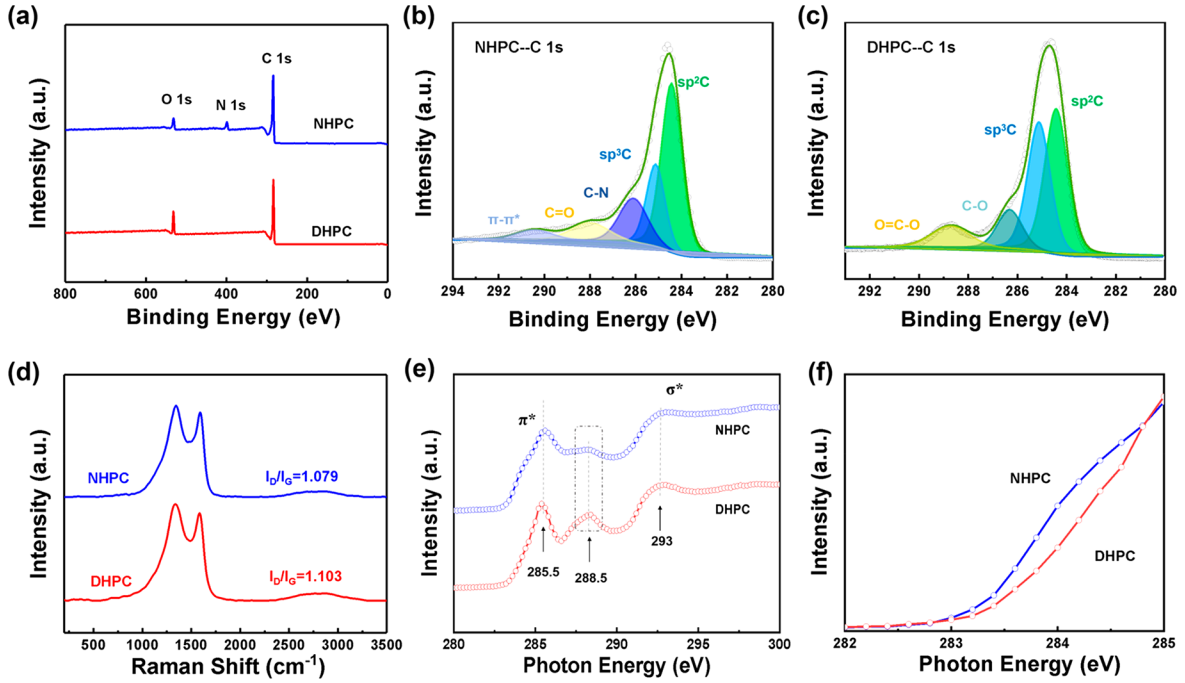

Figure 3. (a) Full XPS spectra of NHPCs and DHPCs. C 1s spectra of (b) NHPCs and (c) DHPCs. (d) Raman profiles of NHPCs and DHPCs. (e) C K-edge NEXAFS spectra for NHPCs and DHPCs and (f) their magnified view between 282 and 285 eV.

the capability of trapping and catalytic conversion of LiPSs without introducing extra components. Recent studies have revealed that intrinsic defect-rich carbon materials possess strong polarity, superior to their heteroatom-doped counterparts. Moreover, these defective sites can essentially facilitate a number of electrochemical reactions including hydrogen evolution reactions, oxygen evolution reactions, oxygen reduction reactions, and carbon dioxide reduction reactions because of the defect-incurred local electronic reconfiguration.[37−39] In this regard, intrinsic defect-rich hierarchically porous carbon architectures (denoted as DHPCs) are supposed to simultaneously fulfill all the requirements raised by Li-S batteries, especially the efficient capture and catalytic conversion of LiPSs. To our knowledge, the potential of such an architecture for this purpose has seldom been verified.

Herein, we report a simple and scalable construction of hierarchically porous carbon architectures with abundant intrinsic defects to host sulfur as the promising cathodes for Li-S batteries. Started from a widely available nitrogen-containing precursor and potassium hydroxide, the nitrogen-doped hierarchically porous carbon architectures (NHPCs) with hexagonally organized macropores possessing micropores and mesopores enriched cellular walls were first prepared by a facile *in situ* templating technology, and the intrinsic defects were then introduced by annealing the NHPCs at a higher temperature. The thus-obtained DHPCs give rationally organized pore structures with uniformly distributed intrinsic defects. The increased polarity and redistributed surface charges at these defective sites offer superior adsorption and robust catalytic conversion toward LiPSs. Moreover, the hierarchically porous architectures permit the full exposure of these active species to the LiPS intermediates, providing sufficient electrochemical interfaces. As a result, the Li-S batteries with DHPCs as the sulfur host offer a high specific capacity of 1182 mAh g^{-1} at a current density of 0.5 C, excellent cycling stability, and outstanding rate capability at a sulfur content of 70 wt %. The facilely regulated carbon architectures may offer an alternative solution to address the detrimental effect of Li-S batteries with promising potential.

RESULTS AND DISCUSSION

The overall synthetic procedure of the DHPCs is exhibited in Figure 1. First, 1,10-phenanthroline and potassium hydroxide at an optimal mass ratio were mixed uniformly by grinding. Then, the mixture was annealed at 800 °C for 2 h in an inert atmosphere to produce NHPCs. Afterward, another annealing procedure at a higher temperature, namely 1150 °C, was conducted, during which the nitrogen in the carbon framework would be essentially removed.[40] The vacancies induced by nitrogen removal at such a high temperature could drive the reorganization of the peripheric carbon atoms, leading to the formation of intrinsic defects of various forms, including pentagons, heptagons, and octagons.

The detailed structure evolution of NHPCs and DHPCs was analyzed using X-ray diffraction (XRD), field-emission scanning electron microscopy (FESEM), and transmission electron microscopy (TEM). As shown in the XRD patterns (Figure S1), both NHPCs and DHPCs present two broad diffraction peaks around 26 and 44°, which can be assigned to the (002) and (101) plane reflections of graphitic carbon, respectively. FESEM observation reveals that NHPCs possess an ultralarge sheet-like morphology (Figure S2a) where the surface is decorated with macropores of around 100−200 nm organized into honeycomb-like patterns (Figure 2a). The possible reasons for the formation of such a structure may be related to the molten environment created by potassium hydroxide at elevated temperatures and the strong chelate effect between 1,10-phenanthroline and metal ions.[41] The wall of the macropores is decorated with multiple mesopores and micropores, revealed from the nitrogen sorption isotherm in Figure S3. After removing nitrogen, the overall morphology of DHPCs is well maintained (Figure S2b). The walls of

https://dx.doi.org/10.1021/acsnano.0c02294
ACS Nano 2020, 14, 6222−6231

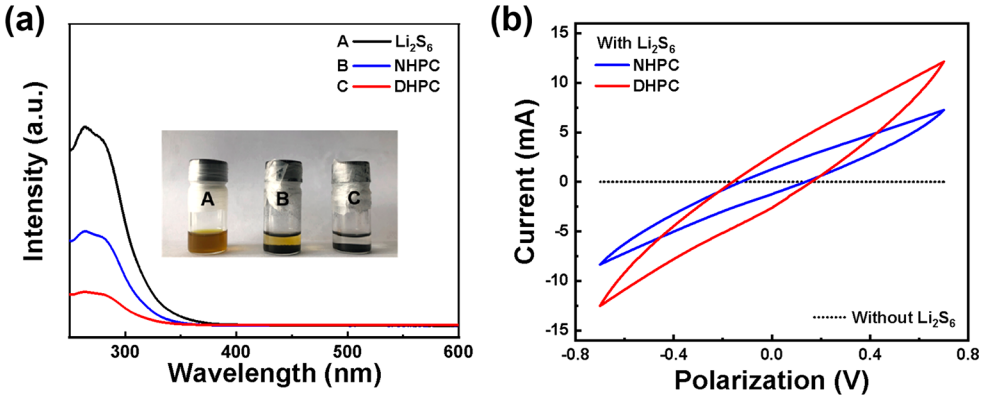

Figure 4. (a) UV−vis absorption spectra of the Li_2S_6 solution before and after adding NHPCs or DHPCs (inset: digital image of pure Li_2S_6 solution and Li_2S_6 solutions after adding NHPCs and DHPCs for 2 h). (b) CV curves of Li_2S_6 symmetric cells employing NHPCs or DHPCs as working electrodes at 50 mV s^{-1}.

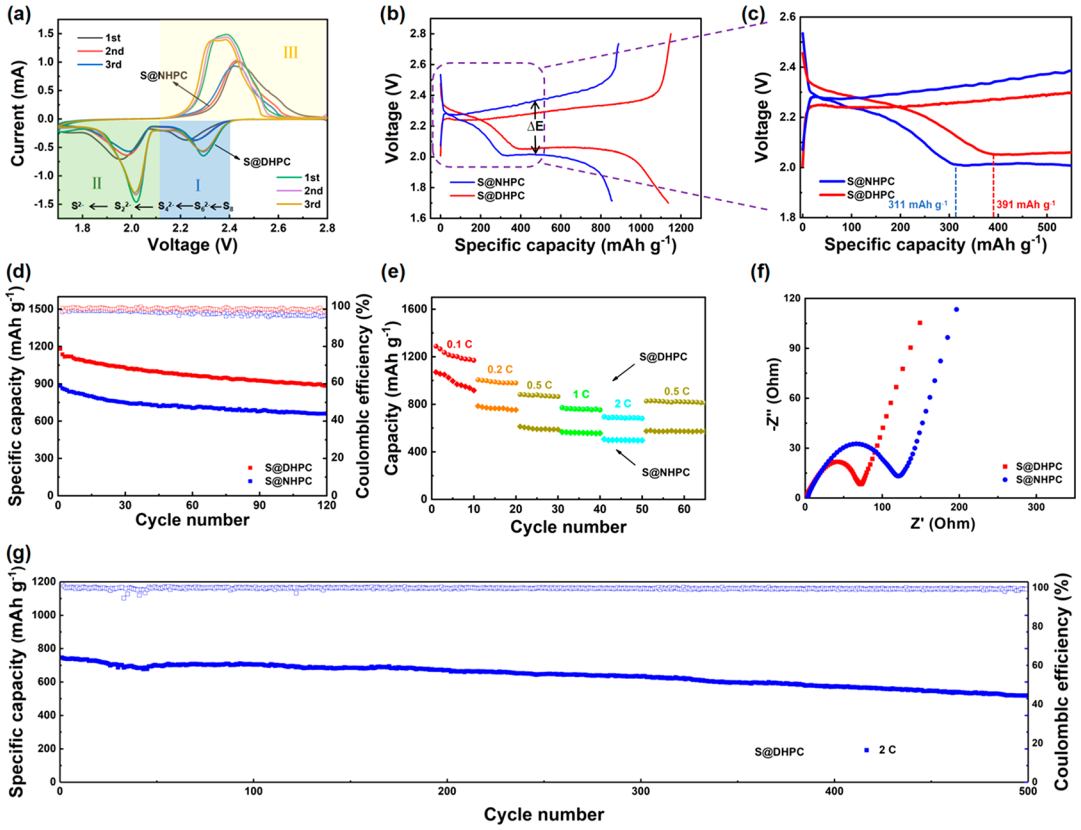

Figure 5. (a) CV curves in a voltage range of 1.7−2.8 V with sweep rate of 0.1 mV s^{-1} and (b) and (c) charge/discharge profiles of S@NHPC and S@DHPC at 0.5 C. (d) Cycling performance at 0.5 C, (e) rate capability, and (f) Nyquist plots of S@NHPC and S@DHPC. (g) Long-term cycling performance of the S@DHPC cathode at 2 C.

macropores in DHPCs, however, are distorted, resulting in a rough surface shown in Figure 2b. The distortion may be associated with the local structural reconstruction after nitrogen removal, and the uniformly distorted structure suggests that the intrinsic defects are evenly distributed throughout the whole network. The structural evolution can be further verified by observing their morphology at higher magnified FESEM (Figure 2c,d) and TEM images (Figure 2e,f). The two structures give very similar nitrogen sorption isotherms, and their specific surface areas are relatively close (Figure S3 and Table S1).

The intrinsic defects were elaborately verified by the combined use of X-ray photoelectron spectroscopy (XPS), Raman spectra, and near-edge X-ray absorption fine structure (NEXAFS) spectroscopy. After the second annealing at 1050 °C, the nitrogen in NHPCs is almost fully removed (Figure 3a, Figure S4, and Table S2), contributing to an increased content of sp^3 carbon (Figure 3b,c). The Raman profiles exhibited in Figure 3d agree well with the XPS results where the intensity of the peak associated with defects at around 1350 cm^{-1} is stronger in DHPCs, giving rise to an increased I_D/I_G ratio, a widely used indicator to describe the relatively defective content in carbon materials.[42,43] Then, C K-edge NEXAFS was

https://dx.doi.org/10.1021/acsnano.0c02294
ACS Nano 2020, 14, 6222−6231

further used to investigate the structural feature (Figure 3e). Compared to NHPCs, DHPCs give a weak shoulder feature around 284.5 eV associated with edge characters (Figure 3e,f), indicative of the increased degree of graphitization in localized regions due to annealing at higher temperatures. This structural feature contributes to the increased conductivity (Table S3).[44] The appearance of a strong peak at 288.5 eV between the π^* (~285.5 eV) and σ^* (~293 eV) resonances in the curve of DHPCs reflects the increase of sp^3-like structures. Due to the decreased edge characters, the origin of intrinsic defects may be located at the basal plane of the graphene domain in carbon materials.[42,45] The emerged intrinsic defects endow the carbon material with a stronger polarity compared to its nitrogen-doped counterpart, reflected from a more hydrophilic surface as shown in Figure S5. As a result, an improved adsorption of the LiPSs can be expected.

To evaluate the adsorption capability of NHPCs and DHPCs toward LiPSs, we carried out visualized adsorption tests and UV−vis absorption measurements as presented in Figure 4a. After adding NHPCs into the Li_2S_6 solution, an obviously weakened color is observed, indicative of the effective adsorption of Li_2S_6 by this nitrogen-doped carbon material. With the same amount of DHPCs introduced, the solution is almost colorless, revealing an enhanced adsorption capacity toward the LiPSs. The UV−vis curves further confirm this conclusion. As shown, the Li_2S_6 solution shows a very strong absorption peak, while the intensity of this peak is reduced after adding NHPCs into this solution. The introduction of DHPCs can induce a much stronger diminution of Li_2S_6-related peak, verifying the significantly enhanced adsorption capability of LiPSs, which is highly desired for the cathode of Li-S batteries.[33] The catalytic activity of the DHPCs and NHPCs toward the conversion of LiPSs in Li-S batteries was compared using symmetric cells with the Li_2S_6-containing electrolyte employing NHPCs and DHPCs as electrodes, separately. Meanwhile, a cell with Li_2S_6-free electrolyte was also evaluated to correct capacitive contributions,[46] which delivers a negligible contribution to the capacitive current. As shown in Figure 4b, the current density of DHPCs cell is much larger than that of NHPCs cell, reflecting that DHPCs promote faster redox reactions for the conversion of LiPSs, shortening their lifespan and thereby further suppressing the notorious shuttle effect.[28,47]

Then, sulfur was impregnated into the carbon architectures as the cathode of Li-S batteries. Even at a loading amount as high as 70 wt % (Figure S6), the sulfur species can still be uniformly distributed as revealed from the elemental mapping (Figure S7). Moreover, the sulfur-related diffraction peaks are almost absent in the XRD pattern of S@DHPC (Figure S8), which is different from the XRD profiles of other sulfur-carbon cathodes.[24] Such a result may unveil a strong anchoring effect of the DHPCs toward sulfur that restrains the heavy aggregation of active species. The electrochemical performances of the Li-S batteries with S@DHPC and S@NHPC cathodes were systematically investigated using cyclic voltammetry (CV), galvanostatic charge−discharge (GCD), and electrochemical impedance spectroscopy (EIS) methods. Figure 5a showcases the CV curves of these two cells recorded at a scan rate of 0.1 mV s^{-1}. In the cathodic branch, two peaks appear where the one at a higher potential (I) results from the reduction of sulfur (S_8) to soluble LiPSs (Li_2S_n, $4 \le n \le 8$) and the peak at the lower potential (II) represents the conversion of LiPSs to insoluble Li_2S_2/Li_2S.[15,48] The area ratio (II/I) of these two cathodic peaks is associated with the conversion degree of the soluble LiPSs to Li_2S, which is widely used to reveal the utilizing ratio of sulfur.[16] The II/I area ratio of S@DHPC was calculated to be 2.05, which is much larger than that of S@NHPSs as well as some previous results,[10,49] suggesting an improved utilization of the active species. In the anodic branch, the overlapped oxidation peaks (III) at around 2.4 V appear which are indicative of the gradual delithiation of Li_2S to LiPSs and eventually to sulfur. The area ratio of the cathodic (I + II)/anodic (III) peaks was calculated to be ~97% for the cell with the S@DHPC cathode, revealing the almost fully reversible conversion of sulfur. As for the S@NHPC cathode, a smaller value is offered, suggesting that the active sulfur is not fully explored. Furthermore, S@DHPC shows a higher reduction potential and lower oxidation potential than the S@NHPC cathode, demonstrating that the intrinsic defects significantly reduce the polarization due to the enhanced catalytic conversion between S and Li_2S.[50] Figure 5b,c presents the typical GCD profiles of S@DHPC and S@NHPC cathodes at a current density of 0.5 C (1 C = 1675 mA g^{-1}). As shown, the discharge branches show two plateaus associated with gradual conversion of S to LiPSs and Li_2S, which coincide with the CV results. Moreover, the reduced polarization by using the S@DHPC cathode is further confirmed by a narrower gap between discharge and charge plateaus. As shown in Figure 5c, a gap of around 0.34 V for the cell with S@NHPC cathode is observed, which is much larger than that of S@DHPC (0.23 V). Furthermore, the S@DHPC-based cell affords a specific capacity of 391 mAh g^{-1} at the first plateau around 2.3 V, comparing favorably to 311 mAh g^{-1} of the S@NHPC. This phenomenon likely arises from the improved interaction between the intrinsic defects and LiPSs, leading to the restriction of their diffusion and enhancement of their reduction.[51] The cycling capability of the S@DHPC and S@NHPC was evaluated at a current density of 0.5 C and compared in Figure 5d. As shown, the S@DHPC cathode displays an initial discharge capacity of 1182 mAh g^{-1}, while the S@NHPC exhibits an initial capacity of only 883 mAh g^{-1}. The specific capacity of the S@NHPC gradually declines to 661 mAh g^{-1} after 120 cycles, much lower than that of S@DHPC where a large specific capacity of 886 mAh g^{-1} is maintained. The rate performance of the cells with different cathodes was also compared at various rates ranging from 0.1 to 2 C as illustrated in Figure 5e. The S@DHPC electrode shows a discharge capacity of 1288, 1005, 884 mAh g^{-1} at the current density of 0.1, 0.2, and 0.5 C, respectively. Even operating the cell at the current density as high as 1 and 2 C, a highly reversible capacity of 771 and 694 mAh g^{-1}, respectively, could still be afforded. When reducing the current density back to 0.5 C, the specific capacity can increase to 826 mAh g^{-1}, indicating the excellent stability of the S@DHPC cathode. In contrast, the S@NHPC electrode delivers much lower capacities under the identical conditions. The GCD curves of the S@DHPC cathode at various current rates in Figure S9 further confirm the improved charge/mass transfer and enhanced active sulfur utilization. Then, the EIS measurement of the two cells was conducted, and the related Nyquist plots of S@DHPC and S@NHPC cathodes are shown in Figure 5f. Obviously, the S@DHPC gives a smaller charge-transfer resistance (R_{ct}), facilitating the enhanced LiPSs conversion.[52] The cycling stability of the S@DHPC cathode was evaluated at 2 C for 500 cycles (Figure 5g). The S@DHPC cathode offers an initial capacity of 746 mAh g^{-1}. After

https://dx.doi.org/10.1021/acsnano.0c02294
ACS Nano 2020, 14, 6222−6231

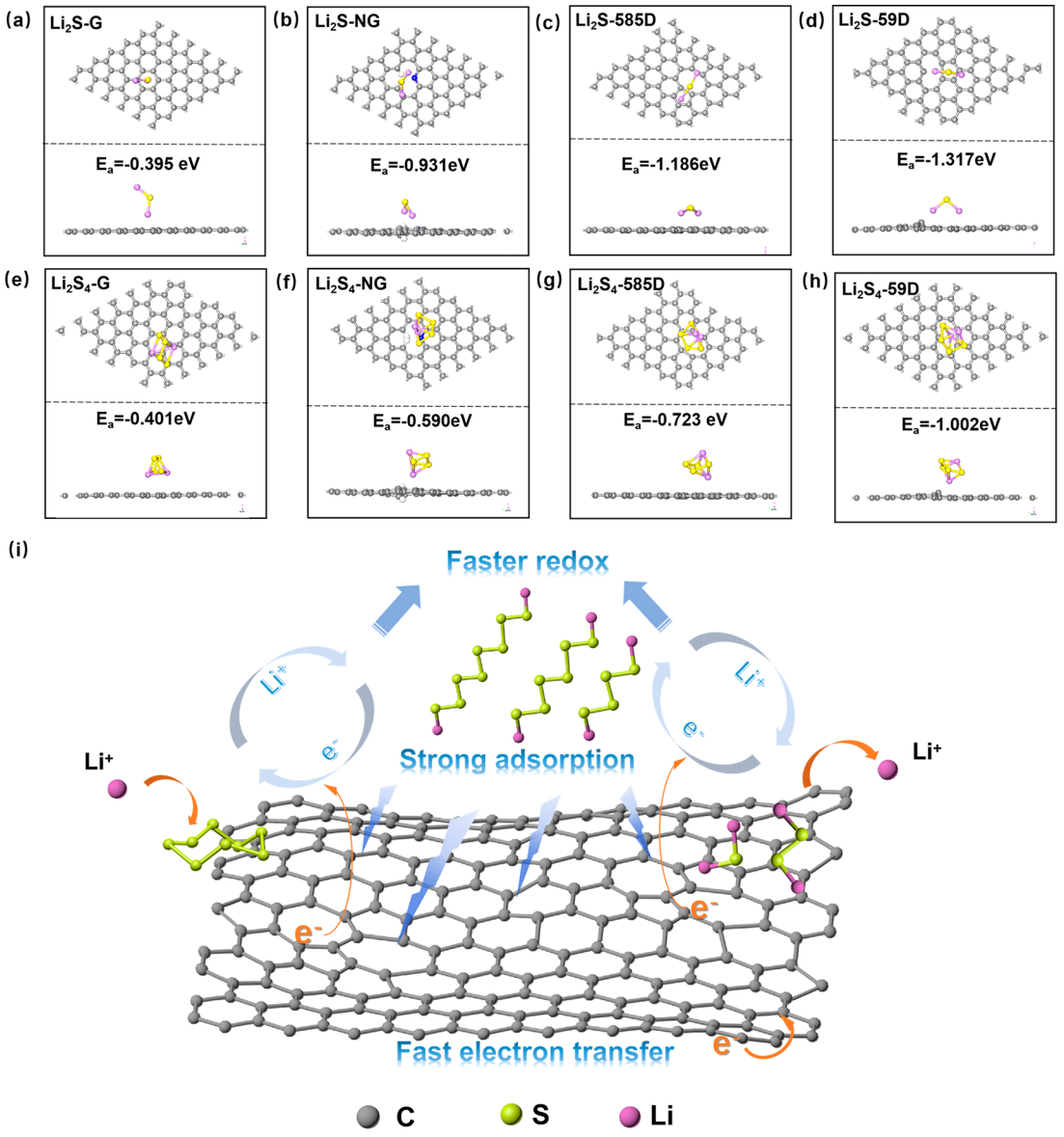

Figure 6. Side and top views of the optimized geometric configurations of Li_2S and Li_2S_4 on (a, e) G, (b, f) NG, (c, g) 585D, and (d, h) 59D. Gray, pink, and yellow balls represent C, Li, and S atoms, respectively. (i) Schematic illustration of the immobilization and conversion of sulfur species on the surface of DHPC.

500 cycles, a reversible discharge specific capacity of 520 mAh g^{-1} still remains, indicative of an average capacity decay rate as low as 0.06% of each cycle. All of these results indicate that the intrinsic defects play a key role in suppressing the shuttle effect and facilitating the chemical conversion of LiPSs, thus rendering a significantly improved performance of the as-fabricated Li-S batteries compared with previously reported results (Table S4). To further explore the synergistic effect of the hierarchical porosity and intrinsic defects, a Li-S battery employing a DHPC-based cathode with a sulfur content as high as 90 wt % (Figure S10a) was assembled for evaluation. As shown in Figure S10b,c, a very decent rate capability can still be afforded. Moreover, a stable cycling performance (Figure S10d) is also obtained which is reflected from a large initial discharge capacity of 873 mAh g^{-1} and a low average capacity fade rate of 0.075% per cycle over 500 cycles.

To get an insight into the improved performance enabled by the intrinsic defect-rich carbon materials, the adsorption behaviors of the Li_2S_n clusters on different types of carbon surfaces have been elucidated by the first-principles calculations. Four types of carbon structures, including pristine graphene (G), pyridinic N-doped graphene (NG), graphene with 5−9 defect (59D), and 5−8−5 defect (585D), were modeled for the theoretical investigation, as illustrated in Figure S11. The adsorption energy E_a is computed to measure the adsorption strength for Li_2S_n species, which is defined as $E_a = E_{Li_2S_n+sub} - E_{Li_2S_n} - E_{sub}$, where $E_{Li_2S_n+sub}$, $E_{Li_2S_n}$, and E_{sub} are the energy of the Li_2S_n substrates systems, the free-standing Li_2S_n, and the carbon substrates, respectively. It is found that the two defective carbons possess a stronger adsorption toward typical sulfur species in Li-S batteries than the N-doped and pristine graphene, as shown in Figure S12, suggesting the improved affinity to LiPSs induced by intrinsic defects. The adsorption of Li_2S (discharge product) and Li_2S_4 (intermediate product) is compared in detail, as shown in Figure 6. Figure 6a−d displays the optimized geometries of Li_2S adsorption on

https://dx.doi.org/10.1021/acsnano.0c02294
ACS Nano 2020, 14, 6222−6231

G, NG, 585D, and 59D. The adsorption energy (E_a) of Li_2S on 585D and 59D is −1.186 and −1.317 eV, respectively, which is more negative than that of G (−0.394 eV) and NG (−0.931 eV), indicative of stronger adsorption of the final discharge products.[47] A similar trend is also found in Figure 6e−h for the optimized geometries of Li_2S_4 on these surfaces, signifying that the intrinsic defects of the carbon can induce improved adsorption for both electron-abundant sulfur and polar sulfur-based anions.

The real-space charge density difference (CDD) (Figure S13) also unveils the much stronger interaction between the defective carbon and sulfur species. Such powerful bonding forces would effectively restrain polysulfide shuttling, leading to long-term stability.[49] To quantitatively unveil the interaction and charge transfer, the Bader charge was applied to obtain the amount of valence electron around each atom of LiPSs. Table S5 lists the variance of charge for each atom in the Li_2S_4 cluster and the Li_2S_4 cluster on different carbon structures where the atomic number of Li_2S_4 is shown in Figure S14. The loss of the electron of Li_2S_4 cluster ($\Delta e_{Li_2S_4}$) is 0.146 and 0.184 e on 59D and 585D, respectively, which is almost 1 order of magnitude larger than those on the G and NG. Thus, 59D and 585D have strong chemical interactions with Li_2S_4, offering an enhanced anchoring effect.[53]

Based on the experimental results and theoretical investigation, the immobilization and conversion of LiPSs on the surface of DHPC are illustrated in Figure 6i. First, the S_8 ring is gradually reduced by electrons and combined with Li^+ ions, giving rise to long-chain LiPSs including Li_2S_6 and Li_2S_4. The intrinsic defects, with strong affinity to LiPSs, can *in situ* trap the as-formed intermediates efficiently. Then, the carbon substrates with facilitated electron transfer would promote the fast conversion of the LiPSs. As a result, this architecture not only restrains the shuttle effect of LiPSs but also promotes their conversion.

CONCLUSION

In summary, we unveil that the intrinsic carbon defects are capable of strong adsorption and superior catalytic conversion of LiPSs. Through a facile two-step annealing method, hierarchically porous carbon architectures rich in these defects could be massively produced at low cost. The existence of intrinsic defects has been elaborately verified by XPS, Raman spectra, and NEXAFS. Based on the experimental and theoretical studies, the essentially improved adsorption and promoted conversion of LiPSs at these defective sites have been elaborately demonstrated. Such a carbon architecture allows a uniform loading of sulfur as high as 90 wt %. The as-synthesized S@DHPCs for Li-S batteries exhibit a high specific capacity of 1182 mAh g^{-1} at 0.5 C, enhanced rate performance, and excellent long-term stability with an ultralow capacity decay of 0.06% per cycle even at a high rate of 2 C. This work could offer an alternative strategy for addressing the detrimental shuttle effect and sluggish conversion kinetics of LiPSs.

EXPERIMENTAL SECTION

Synthesis of NHPCs. In a typical synthesis, 1,10-phenanthroline monohydrate (Aladdin Ltd.) and KOH (Sinopharm Ltd.) with a mass ratio of 1:4 were ground by hand in an agate mortar for 5 min. The mixture was then put in a corundum boat and heated in a tube furnace under an inert atmosphere at 800 °C for 2 h with a heating rate of 5 °C min^{-1}. After repeatedly washing with the dilute HCl solution (10%) and distilled water and subsequently drying at 60 °C for 10 h, the NHPCs were obtained.

Synthesis of DHPCs. The DHPCs were prepared by simply annealing the as-obtained NHPCs at a higher temperature. Specifically, NHPCs were annealed at a high temperature of 1150 °C for 2 h with a ramp rate of 5 °C min^{-1} in nitrogen atmosphere *via* which the nitrogen atoms in NHPCs could be essentially subtracted, giving rise to the intrinsic defect-rich carbon materials.

Synthesis of S@NHPC and S@DHPC. The as-prepared host materials and sublimed sulfur powder in mass ratios of around either 30:70 or 10:90 were added into the CS_2 solvent to produce uniform dispersions. Then, the dispersions were stirred at 45 °C to evaporate CS_2. After that, the as-obtained samples were sealed in vacuum glass tubes, which were then kept at 155 °C for 12 h. Another heat treatment at 200 °C for 2 h under an inert condition was conducted, *via* which the redundant sulfur on the exterior surface of the composites would be removed, giving rise to S@NHPC and S@DHPC.

Material Characterizations. Crystal structure characterization was carried out with XRD on an X'Pert PRO MPD system. FESEM (S4800 from Hitachi, Japan) and TEM (JEM-2100UHR, Japan) were employed to analyze the morphology and structure evolution. The nitrogen sorption isotherms of the NHPCs and DHPCs were recorded on a gas adsorption apparatus (ASAP 2020, Micromeritics, USA) to produce the specific surface area and pore size distribution. Electrical conductivity was measured using the four-probe method on the ST-2777 resistivity of power tester. The sulfur content was measured by recording the thermogravimetric curves of the sulfur/carbon composites from ambient temperature to 600 °C with a ramping rate of 10 °C min^{-1} under nitrogen atmosphere on a thermal gravimetric analyzer (Q500, TQ, USA). The elemental mapping of S@DHPC was analyzed using TEM (JEM-2100F) equipped with energy-dispersive X-ray spectroscopy (AZtecOne, Oxford Instrument, UK). The structure defects were then systematically analyzed using different technologies including Raman spectroscopy (RM2000, Renishaw, UK), XPS (Escalab 250XI, Thermo Scientific, USA), NEXAFS at Beijing Synchrotron Radiation Facility equipped with a hemispherical electron analyzer, and a microchannel plate detector.

LiPSs Adsorption Evaluation. First, a homogeneous solution with 2 mM Li_2S_6 solution was prepared by dissolving sublimed sulfur and Li_2S in a molar ratio of 5:1 in 1,2-dimethoxyethane and 1,3-dioxolane (DME/DOL, 1:1 vol) at 55 °C for 12 h under vigorous stirring. The process was carried out in an Ar-filled glovebox. Then, the UV−vis spectra of the solution before and after adding NHPCs/DHPCs were recorded using a UV−vis spectrophotometer (UV-2700, Shimadzu, Japan).

Electrochemical Measurements. The electrodes of the symmetric cell, which were employed for kinetic analysis, were prepared by casting the slurry containing the as-prepared carbon materials, carbon black, and polyvinylidene difluoride with a mass ratio of 7:2:1 on aluminum foil and then cut into disks of 12 mm in diameter. Two identical electrodes were used to assemble the symmetric cell where 40 μL of the electrolyte containing 0.5 M Li_2S_6 and 1 M lithium bis(trifluoromethanesulfonyl) imide (LiTFSI) dissolved in DOL/DME (1:1 in volume) was added in each cell. The CV curves were recorded on an electrochemical workstation (Ivium-n-Stat, Ivium Technologies, The Netherlands) at a scan rate of 50 mV s^{-1}. As for the cathode performance of Li-S batteries, the as-prepared working electrode containing the sulfur/carbon composites, carbon black, and polyvinylidene difluoride in a mass ratio of 7:2:1 and a pure Li foil as the reference and counter electrode were assembled into a cell in an Ar-filled glovebox. The loading mass of the active species in the working electrodes was around 1.5−2.0 mg cm^{-2}. These two electrodes were separated by a microporous polypropylene membrane and infiltrated with an electrolyte containing 1.0 M LiTFSI in DME/DOL (1:1 in volume) with 1.0% $LiNO_3$. The GCD tests were performed on a Land Battery Measurement System (CT2001A, LANHE, China) at a current density ranging from 0.1 to 2 C (1 C = 1675 mA g^{-1}) between 1.7 and 2.8 V *vs* Li/Li^+. The specific capacity calculated in this work was based on the mass of sulfur in the cathode.

https://dx.doi.org/10.1021/acsnano.0c02294
ACS Nano 2020, 14, 6222−6231

CV curves were recorded on an electrochemical workstation (Ivium-n-Stat, Ivium Technologies, The Netherlands) in the voltage window of 1.7 and 2.8 V at a scan rate of 0.1 mV s^{-1}. The EIS evaluation of the cells was obtained using an impedance analyzer (PARSTAT4000, Ameteksi, USA) in the frequency range between 100 kHz and 10 mHz where the voltage amplitude is 10 mV.

Theoretical Calculations. The Vienna *ab initio* simulation package based on density functional theory (DFT) was employed to perform the computations.[54,55] The projector augmented wave method with an energy cutoff of 500 eV was used for modeling. The generalized gradient approximation exchange−correlation function was used in Perdew−Burke−Ernzerhof form.[56] DFT-D3 functional was used to describe the van der Waals interaction.[57] The total energy change was converged to within 10^{-5} eV, and the atomic configuration was completely relaxed until the maximum residual of force becomes <0.02 eV $Å^{-1}$. K-points were adjusted as 3 × 3 × 1 by the Monkhorst−Pack method.[58] To avoid the unexpected interactions between atoms in the periodic super cells, a layer thickness of 25 Å was set as the vacuum condition. A 6 × 6 unit cell of graphene was employed for all the configurations. The defect may exist in different configurations. Here, we investigated two defects configurations and a possible pyridinic N doping configuration. The 5−9 defect was created by removal of single atom from the graphene lattice, while the 5−8−5 defect was realized by the removal of two atoms from the graphene.[59] The attention was focused on the adsorption behavior of typical sulfur-related species in Li-S batteries including S_8, Li_2S_8, Li_2S_6, Li_2S_4, Li_2S_2, and Li_2S on these substrates.

ASSOCIATED CONTENT

Supporting Information

The Supporting Information is available free of charge at https://pubs.acs.org/doi/10.1021/acsnano.0c02294.

XRD patterns of NHPCs and DHPCs; additional SEM images of NHPCs and DHPCs; N_2 sorption isotherms and pore size distribution of these two carbon materials; elemental mapping and XRD pattern of S@DHPC; XPS, electrical conductivity, and water contact angle of NHPCs and DHPCs; TGA curves of S@NHPC and S@DHPC; first charge/discharge profiles of S@DHPC cathode at various current rates and electrochemical analysis of the S@DHPC at a sulfur loading of 90 wt %; comparison of the electrochemical performance of present work with previously reported results; detailed information on DFT including atomic structure, adsorption energies, charge density difference, and Bader charge difference (PDF)

AUTHOR INFORMATION

Corresponding Authors

Han Hu − *State Key Laboratory of Heavy Oil Processing, Institute of New Energy, College of Chemical Engineering, China University of Petroleum (East China), Qingdao 266580, China;* orcid.org/0000-0002-3755-7342; Email: hhu@upc.edu.cn

Mingbo Wu − *State Key Laboratory of Heavy Oil Processing, Institute of New Energy, College of Chemical Engineering, China University of Petroleum (East China), Qingdao 266580, China;* orcid.org/0000-0003-0048-778X; Email: wumb@upc.edu.cn

Authors

Lu Guan − *State Key Laboratory of Heavy Oil Processing, Institute of New Energy, College of Chemical Engineering, China University of Petroleum (East China), Qingdao 266580, China*

Linqing Li − *State Key Laboratory of Heavy Oil Processing, Institute of New Energy, College of Chemical Engineering, China University of Petroleum (East China), Qingdao 266580, China*

Yuanyuan Pan − *State Key Laboratory of Heavy Oil Processing, Institute of New Energy, College of Chemical Engineering, China University of Petroleum (East China), Qingdao 266580, China;* orcid.org/0000-0003-1368-2496

Yifan Zhu − *State Key Laboratory of Heavy Oil Processing, Institute of New Energy, College of Chemical Engineering, China University of Petroleum (East China), Qingdao 266580, China*

Qiang Li − *College of Physics Science, Qingdao University, Qingdao 266071, China*

Hailing Guo − *State Key Laboratory of Heavy Oil Processing, Institute of New Energy, College of Chemical Engineering, China University of Petroleum (East China), Qingdao 266580, China;* orcid.org/0000-0002-5211-5462

Kai Wang − *College of Electrical Engineering, Qingdao University, Qingdao 266071, China;* orcid.org/0000-0002-3513-3511

Yunchun Huang − *State Key Laboratory of Heavy Oil Processing, Institute of New Energy, College of Chemical Engineering, China University of Petroleum (East China), Qingdao 266580, China*

Mengdi Zhang − *State Key Laboratory of Heavy Oil Processing, Institute of New Energy, College of Chemical Engineering, China University of Petroleum (East China), Qingdao 266580, China*

Yingchun Yan − *State Key Laboratory of Heavy Oil Processing, Institute of New Energy, College of Chemical Engineering, China University of Petroleum (East China), Qingdao 266580, China*

Zhongtao Li − *State Key Laboratory of Heavy Oil Processing, Institute of New Energy, College of Chemical Engineering, China University of Petroleum (East China), Qingdao 266580, China;* orcid.org/0000-0003-0157-6098

Xiaoling Teng − *State Key Laboratory of Heavy Oil Processing, Institute of New Energy, College of Chemical Engineering, China University of Petroleum (East China), Qingdao 266580, China*

Junwei Yang − *State Key Laboratory of Heavy Oil Processing, Institute of New Energy, College of Chemical Engineering, China University of Petroleum (East China), Qingdao 266580, China;* orcid.org/0000-0003-1673-3017

Jiazhi Xiao − *State Key Laboratory of Heavy Oil Processing, Institute of New Energy, College of Chemical Engineering, China University of Petroleum (East China), Qingdao 266580, China;* orcid.org/0000-0002-6048-3417

Yunlong Zhang − *State Key Laboratory of Heavy Oil Processing, Institute of New Energy, College of Chemical Engineering, China University of Petroleum (East China), Qingdao 266580, China*

Xiaoshan Wang − *State Key Laboratory of Heavy Oil Processing, Institute of New Energy, College of Chemical Engineering, China University of Petroleum (East China), Qingdao 266580, China*

Complete contact information is available at: https://pubs.acs.org/10.1021/acsnano.0c02294

Notes

The authors declare no competing financial interest.

ACKNOWLEDGMENTS

This work was financially supported by National Natural Science Foundation of China (21975287, 11904409), the startup support grant from China University of Petroleum

(East China), Technological Leading Scholar of 10000 Talent Project (no. W03020508), Taishan Scholar Project (no. ts201712020), and Shandong Provincial Natural Science Foundation (ZR2018ZC1458).

REFERENCES

(1) Bruce, P. G.; Freunberger, S. A.; Hardwick, L. J.; Tarascon, J.-M. Li-O_2 and Li-S Batteries with High Energy Storage. *Nat. Mater.* **2012**, *11*, 19−29.
(2) Zhao, X.; Cai, W.; Yang, Y.; Song, X.; Neale, Z.; Wang, H. E.; Sui, J.; Cao, G. $MoSe_2$ Nanosheets Perpendicularly Grown on Graphene with Mo-C Bonding for Sodium-Ion Capacitors. *Nano Energy* **2018**, *47*, 224−234.
(3) Pomerantseva, E.; Bonaccorso, F.; Feng, X.; Cui, Y.; Gogotsi, Y. Energy Storage: The Future Enabled by Nanomaterials. *Science* **2019**, *366*, No. eaan8285.
(4) Cheng, F.; Liang, J.; Tao, Z.; Chen, J. Functional Materials for Rechargeable Batteries. *Adv. Mater.* **2011**, *23*, 1695−1715.
(5) Pang, Q.; Liang, X.; Kwok, C. Y.; Nazar, L. F. Advances in Lithium-Sulfur Batteries Based on Multifunctional Cathodes and Electrolytes. *Nat. Energy* **2016**, *1*, 16132.
(6) Yu, M.; Wang, Z.; Wang, Y.; Dong, Y.; Qiu, J. Freestanding Flexible Li_2S Paper Electrode with High Mass and Capacity Loading for High-Energy Li-S Batteries. *Adv. Energy Mater.* **2017**, *7*, 1700018.
(7) Ye, C.; Chao, D.; Shan, J.; Li, H.; Davey, K.; Qiao, S. Z. Unveiling the Advances of 2D Materials for Li/Na-S Batteries Experimentally and Theoretically. *Matter* **2020**, *2*, 323−344.
(8) Manthiram, A.; Fu, Y.; Chung, S. H.; Zu, C.; Su, Y. S. Rechargeable Lithium-Sulfur Batteries. *Chem. Rev.* **2014**, *114*, 11751−11787.
(9) Zhang, M.; Yu, C.; Yang, J.; Zhao, C.; Ling, Z.; Qiu, J. Nitrogen-Doped Tubular/Porous Carbon Channels Implanted on Graphene Frameworks for Multiple Confinement of Sulfur and Polysulfides. *J. Mater. Chem. A* **2017**, *5*, 10380−10386.
(10) Ren, J.; Xia, L.; Zhou, Y.; Zheng, Q.; Liao, J.; Lin, D. A Reduced Graphene Oxide/Nitrogen, Phosphorus Doped Porous Carbon Hybrid Framework as Sulfur Host for High Performance Lithium-Sulfur Batteries. *Carbon* **2018**, *140*, 30−40.
(11) Seh, Z. W.; Sun, Y.; Zhang, Q.; Cui, Y. Designing High-Energy Lithium-Sulfur Batteries. *Chem. Soc. Rev.* **2016**, *45*, 5605−5634.
(12) Fang, R.; Zhao, S.; Sun, Z.; Wang, D. W.; Cheng, H. M.; Li, F. More Reliable Lithium-Sulfur Batteries: Status, Solutions and Prospects. *Adv. Mater.* **2017**, *29*, 1606823.
(13) Huang, J.; Zhai, P.; Peng, H.; Zhu, W.; Zhang, Q. Metal/Nanocarbon Layer Current Collectors Enhanced Energy Efficiency in Lithium-Sulfur Batteries. *Sci. Bull.* **2017**, *62*, 1267−1274.
(14) Xie, J.; Li, B. Q.; Peng, H. J.; Song, Y. W.; Zhao, M.; Chen, X.; Zhang, Q.; Huang, J. Q. Implanting Atomic Cobalt within Mesoporous Carbon toward Highly Stable Lithium-Sulfur Batteries. *Adv. Mater.* **2019**, *31*, 1903813.
(15) Liang, J.; Sun, Z. H.; Li, F.; Cheng, H. M. Carbon Materials for Li-S Batteries: Functional Evolution and Performance Improvement. *Energy Storage Mater.* **2016**, *2*, 76−106.
(16) Fang, R.; Zhao, S.; Hou, P.; Cheng, M.; Wang, S.; Cheng, H. M.; Liu, C.; Li, F. 3D Interconnected Electrode Materials with Ultrahigh Areal Sulfur Loading for Li-S Batteries. *Adv. Mater.* **2016**, *28*, 3374.
(17) Fang, R.; Zhao, S.; Pei, S.; Qian, X.; Hou, P. X.; Cheng, H. M.; Liu, C.; Li, F. Toward More Reliable Lithium-Sulfur Batteries: An All-Graphene Cathode Structure. *ACS Nano* **2016**, *10*, 8676−8682.
(18) Zhou, W.; Xiao, X.; Cai, M.; Yang, L. Polydopamine-Coated, Nitrogen-Doped, Hollow Carbon-Sulfur Double-Layered Core-Shell Structure for Improving Lithium-Sulfur Batteries. *Nano Lett.* **2014**, *14*, 5250−5256.
(19) Gueon, D.; Hwang, J. T.; Yang, S. B.; Cho, E.; Sohn, K.; Yang, D. K.; Moon, J. H. Spherical Macroporous Carbon Nanotube Particles with Ultrahigh Sulfur Loading for Lithium-Sulfur Battery Cathodes. *ACS Nano* **2018**, *12*, 226−232.
(20) Xu, Z. L.; Kim, J. K.; Kang, K. Carbon Nanomaterials for Advanced Lithium Sulfur Batteries. *Nano Today* **2018**, *19*, 84−107.
(21) Li, Z.; Li, C.; Ge, X.; Ma, J.; Zhang, Z.; Li, Q.; Wang, C.; Yin, L. Reduced Graphene Oxide Wrapped MOFs-Derived Cobalt-Doped Porous Carbon Polyhedrons as Sulfur Immobilizers as Cathodes for High Performance Lithium Sulfur Batteries. *Nano Energy* **2016**, *23*, 15−26.
(22) Zhang, S. S. Heteroatom-Doped Carbons: Synthesis, Chemistry and Application in Lithium/Sulphur Batteries. *Inorg. Chem. Front.* **2015**, *2*, 1059−1069.
(23) Li, S.; Mou, T.; Ren, G.; Warzywoda, J.; Wang, B.; Fan, Z. Confining Sulfur Species in Cathodes of Lithium-Sulfur Batteries: Insight into Nonpolar and Polar Matrix Surfaces. *ACS Energy Lett.* **2016**, *1*, 481−489.
(24) Wang, Z.; Dong, Y.; Li, H.; Zhao, Z.; Bin Wu, H.; Hao, C.; Liu, S.; Qiu, J.; Lou, X. W. Enhancing Lithium-Sulphur Battery Performance by Strongly Binding the Discharge Products on Amino-Functionalized Reduced Graphene Oxide. *Nat. Commun.* **2014**, *5*, 5002.
(25) Xu, J.; Zhang, W.; Fan, H.; Cheng, F.; Su, D.; Wang, G. Promoting Lithium Polysulfide/Sulfide Redox Kinetics by the Catalyzing of Zinc Sulfide for High Performance Lithium-Sulfur Battery. *Nano Energy* **2018**, *51*, 73−82.
(26) Ma, L.; Zhang, W.; Wang, L.; Hu, Y.; Zhu, G.; Wang, Y.; Chen, R.; Chen, T.; Tie, Z.; Liu, J.; Jin, Z. Strong Capillarity, Chemisorption, and Electrocatalytic Capability of Crisscrossed Nanostraws Enabled Flexible, High-Rate, and Long-Cycling Lithium-Sulfur Batteries. *ACS Nano* **2018**, *12*, 4868−4876.
(27) Song, Y.; Zhao, W.; Kong, L.; Zhang, L.; Zhu, X.; Shao, Y.; Ding, F.; Zhang, Q.; Sun, J.; Liu, Z. Synchronous Immobilization and Conversion of Polysulfides on a VO_2-VN Binary Host Targeting High Sulfur Load Li-S Batteries. *Energy Environ. Sci.* **2018**, *11*, 2620−2630.
(28) Wang, Y.; Zhang, R.; Pang, Y. C.; Chen, X.; Lang, J.; Xu, J.; Xiao, C.; Li, H.; Xi, K.; Ding, S. Carbon@Titanium Nitride Dual Shell Nanospheres as Multi-Functional Hosts for Lithium Sulfur Batteries. *Energy Storage Mater.* **2019**, *16*, 228.
(29) Yao, M.; Wang, Y.; Zhao, Z.; Liu, Y.; Niu, Z.; Chen, J. A Flexible All-in-One Lithium-Sulfur Battery. *ACS Nano* **2018**, *12*, 12503.
(30) Li, Z.; Zhang, J.; Lou, X. W. Hollow Carbon Nanofibers Filled with MnO_2 Nanosheets as Efficient Sulfur Hosts for Lithium-Sulfur Batteries. *Angew. Chem., Int. Ed.* **2015**, *54*, 12886−12890.
(31) Huang, X.; Tang, J.; Luo, B.; Knibbe, R.; Lin, T.; Hu, H.; Rana, M.; Hu, Y.; Zhu, X.; Gu, Q.; Wang, D.; Wang, L. Sandwich-Like Ultrathin TiS_2 Nanosheets Confined within N, S Codoped Porous Carbon as an Effective Polysulfide Promoter in Lithium-Sulfur Batteries. *Adv. Energy Mater.* **2019**, *9*, 1901872.
(32) Ye, C.; Zhang, L.; Guo, C. X.; Li, D. D.; Vasileff, A.; Wang, H. H.; Qiao, S. Z. A 3D Hybrid of Chemically Coupled Nickel Sulfide and Hollow Carbon Spheres for High Performance Lithium-Sulfur Batteries. *Adv. Funct. Mater.* **2017**, *27*, 1702524.
(33) Zhang, B.; Luo, C.; Deng, Y.; Huang, Z.; Zhou, G.; Lv, W.; He, Y. B.; Wan, Y.; Kang, F.; Yang, Q. H. Optimized Catalytic WS_2-WO_3 Heterostructure Design for Accelerated Polysulfide Conversion in Lithium-Sulfur Batteries. *Adv. Energy Mater.* **2020**, *10*, 2000091.
(34) Huang, S.; Lim, Y. V.; Zhang, X.; Wang, Y.; Zheng, Y.; Kong, D.; Ding, M.; Yang, S. A.; Yang, H. Regulating the Polysulfide Redox Conversion by Iron Phosphide Nanocrystals for High-Rate and Ultrastable Lithium-Sulfur Battery. *Nano Energy* **2018**, *51*, 340−348.
(35) Zhou, G.; Tian, H.; Jin, Y.; Tao, X.; Liu, B.; Zhang, R.; Seh, Z. W.; Zhuo, D.; Liu, Y.; Sun, J.; Zhao, J.; Zu, C.; Wu, D. S.; Zhang, Q.; Cui, Y. Catalytic Oxidation of Li_2S on the Surface of Metal Sulfides for Li-S Batteries. *Proc. Natl. Acad. Sci. U. S. A.* **2017**, *114*, 840−845.
(36) Pang, Q.; Kwok, C. Y.; Kundu, D.; Liang, X.; Nazar, L. F. Lightweight Metallic MgB_2 Mediates Polysulfide Redox and Promises High-Energy Density Lithium-Sulfur Batteries. *Joule* **2019**, *3*, 136−148.

https://dx.doi.org/10.1021/acsnano.0c02294
ACS Nano 2020, 14, 6222−6231

(37) Yan, X. C.; Jia, Y.; Yao, X. D. Defects on Carbons for Electrocatalytic Oxygen Reduction. *Chem. Soc. Rev.* **2018**, *47*, 7628−7658.
(38) Zhang, Y.; Tao, L.; Xie, C.; Wang, D.; Zou, Y.; Chen, R.; Wang, Y.; Jia, C.; Wang, S. Defect Engineering on Electrode Materials for Rechargeable Batteries. *Adv. Mater.* **2020**, *32*, 1905923.
(39) Wu, Q.; Yang, L.; Wang, X.; Hu, Z. Carbon-Based Nanocages: A New Platform for Advanced Energy Storage and Conversion. *Adv. Mater.* **2019**, 1904177.
(40) Jia, Y.; Zhang, L.; Du, A.; Gao, G.; Chen, J.; Yan, X.; Brown, C. L.; Yao, X. Defect Graphene as a Trifunctional Catalyst for Electrochemical Reactions. *Adv. Mater.* **2016**, *28*, 9532.
(41) Li, M.; Liu, C.; Cao, H.; Zhao, H.; Zhang, Y.; Fan, Z. KOH Self-Templating Synthesis of Three-Dimensional Hierarchical Porous Carbon Materials for High Performance Supercapacitors. *J. Mater. Chem. A* **2014**, *2*, 14844−14851.
(42) Milev, A.; Tran, N.; Kannangara, K.; Wilson, M. Influence of Bond Defects on Coiling of Graphite. *Sci. Technol. Adv. Mater.* **2006**, *7*, 834.
(43) Jiang, Y.; Yang, L.; Sun, T.; Zhao, J.; Lyu, Z.; Zhuo, O.; Wang, X.; Wu, Q.; Ma, J.; Hu, Z. Significant Contribution of Intrinsic Carbon Defects to Oxygen Reduction Activity. *ACS Catal.* **2015**, *5*, 6707−6712.
(44) Wang, W.; Shang, L.; Chang, G.; Yan, C.; Shi, R.; Zhao, Y.; Waterhouse, G. I. N.; Yang, D.; Zhang, T. Intrinsic Carbon Defect-Driven Electrocatalytic Reduction of Carbon Dioxide. *Adv. Mater.* **2019**, *31*, 1808276.
(45) Dong, Y.; Zhang, S.; Du, X.; Hong, S.; Zhao, S.; Chen, Y.; Chen, X.; Song, H. Boosting the Electrical Double-Layer Capacitance of Graphene by Self-Doped Defects through Ball-Milling. *Adv. Funct. Mater.* **2019**, *29*, 1901127.
(46) Lin, H.; Yang, L.; Jiang, X.; Li, G.; Zhang, T.; Yao, Q.; Zheng, G. W.; Lee, J. Y. Electrocatalysis of Polysulfide Conversion by Sulfur-Deficient MoS_2 Nanoflakes for Lithium-Sulfur Batteries. *Energy Environ. Sci.* **2017**, *10*, 1476−1486.
(47) Yang, W.; Yang, W.; Dong, L.; Gao, X.; Wang, G.; Shao, G. Enabling Immobilization and Conversion of Polysulfides through a Nitrogen-Doped Carbon Nanotubes/Ultrathin MoS_2 Nanosheet Core-Shell Architecture for Lithium-Sulfur Batteries. *J. Mater. Chem. A* **2019**, *7*, 13103−13112.
(48) Xiao, D.; Lu, C.; Chen, C.; Yuan, S. CeO_2-Webbed Carbon Nanotubes as a Highly Efficient Sulfur Host for Lithium-Sulfur Batteries. *Energy Storage Mater.* **2018**, *10*, 216−222.
(49) Ai, W.; Li, J.; Du, Z.; Zou, C.; Du, H.; Xu, X.; Chen, Y.; Zhang, H.; Zhao, J.; Li, C.; Huang, W.; Yu, T. Dual Confinement of Polysulfides in Boron-Doped Porous Carbon Sphere/Graphene Hybrid for Advanced Li-S Batteries. *Nano Res.* **2018**, *11*, 4562−4573.
(50) Liu, Y. T.; Han, D. D.; Wang, L.; Li, G. R.; Liu, S.; Gao, X. P. $NiCo_2O_4$ Nanofibers as Carbon-Free Sulfur Immobilizer to Fabricate Sulfur-Based Composite with High Volumetric Capacity for Lithium-Sulfur Battery. *Adv. Energy Mater.* **2019**, *9*, 1803477.
(51) Yang, X.; Gao, X.; Sun, Q.; Jand, S. P.; Yu, Y.; Zhao, Y.; Li, X.; Adair, K.; Kuo, L. Y.; Rohrer, J.; Liang, J.; Lin, X.; Banis, M. N.; Hu, Y.; Zhang, H.; Li, X.; Li, R.; Zhang, H.; Kaghazchi, P.; Sham, T.; et al. Promoting the Transformation of Li_2S_2 to Li_2S: Significantly Increasing Utilization of Active Materials for High-Sulfur-Loading Li-S Batteries. *Adv. Mater.* **2019**, *31*, 1901220.
(52) Sun, W.; Liu, C.; Li, Y.; Luo, S.; Liu, S.; Hong, X.; Xie, K.; Liu, Y.; Tan, X.; Zheng, C. Rational Construction of Fe_2N@C Yolk-Shell Nanoboxes as Multifunctional Hosts for Ultralong Lithium-Sulfur Batteries. *ACS Nano* **2019**, *13*, 12137−12147.
(53) Zhang, Q.; Wang, Y.; Seh, Z. W.; Fu, Z.; Zhang, R.; Cui, Y. Understanding the Anchoring Effect of Two-Dimensional Layered Materials for Lithium-Sulfur Batteries. *Nano Lett.* **2015**, *15*, 3780−3786.
(54) Kresse, G.; Hafner, J. *Ab Initio* Molecular Dynamics for Open-Shell Transition Metals. *Phys. Rev. B: Condens. Matter Mater. Phys.* **1993**, *48*, 13115−13118.
(55) Kresse, G.; Furthmuller, J. Efficient Iterative Schemes for *Ab Initio* Total-Energy Calculations Using a Plane-Wave Basis Set. *Phys. Rev. B: Condens. Matter Mater. Phys.* **1996**, *54*, 11169−11186.
(56) Blochl, P. E. Projector Augmented-Wave Method. *Phys. Rev. B: Condens. Matter Mater. Phys.* **1994**, *50*, 17953−17979.
(57) Klimes, J.; Bowler, D. R.; Michaelides, A. J. Chemical Accuracy for the van der Waals Density Functional. *J. Phys.: Condens. Matter* **2010**, *22*, 022201.
(58) Monkhorst, H. J.; Pack, J. D. Special Points for Brillouin-Zone Integrations. *Phys. Rev. B* **1976**, *13*, 5188−5192.
(59) Banhart, F.; Kotakoski, J.; Krasheninnikov, A. Structural Defects in Graphene. *ACS Nano* **2011**, *5*, 26−41.

https://dx.doi.org/10.1021/acsnano.0c02294
ACS Nano 2020, 14, 6222−6231